

1 CO<sub>2</sub> storage and release in the deep Southern Ocean on  
2 millennial to centennial timescales

3 Rae, J.W.B.<sup>1,\*</sup>, Burke, A.<sup>1</sup>, Robinson, L.F.<sup>2</sup>, Adkins, J.F.<sup>3</sup>, Chen, T.<sup>2,4</sup>, Cole,  
4 C.<sup>1</sup>, Greenop, R.<sup>1</sup>, Li, T.<sup>2,4</sup>, Littley, E.<sup>1</sup>, Nita, D.C.<sup>1,5</sup>, Stewart, J.A.<sup>1,2</sup>, Taylor,  
5 B<sup>1</sup>.

6 1. School of Earth and Environmental Sciences, University of St Andrews, UK.

7 2. School of Earth Sciences, University of Bristol, UK

8 3. Division of Geological and Planetary Sciences, California Institute of  
9 Technology, USA

10 4. School of Earth Sciences and Engineering, Nanjing University, China

11 5. Faculty of Environmental Science and Engineering, Babes-Bolyai  
12 University, Cluj-Napoca, Romania

13

14 The cause of atmospheric CO<sub>2</sub> change during the recent ice ages remains a  
15 first order question in climate science. Most mechanisms have invoked  
16 carbon exchange with the deep ocean, due to its large size and relatively  
17 rapid exchange time with the atmosphere <sup>1</sup>. The Southern Ocean is thought  
18 to play a key role in this exchange, as much of the deep ocean is ventilated to  
19 the atmosphere in this region <sup>2</sup>. However reconstructing changes in deep  
20 Southern Ocean carbon storage is challenging, so **few direct tests of this**  
21 **hypothesis exist. Here we present new deep-sea coral boron isotope**  
22 **data that track the pH – and thus CO<sub>2</sub> chemistry – of the deep Southern**  
23 **Ocean over the last 40,000 years. At sites closest to the Antarctic**  
24 **continental margin, and most influenced by the deep Southern waters**  
25 **that form the ocean's lower overturning cell, we find a close relationship**  
26 **between ocean pH and atmospheric CO<sub>2</sub>: during intervals of low CO<sub>2</sub>**  
27 **ocean pH is low, reflecting enhanced ocean carbon storage; during**  
28 **intervals of rising CO<sub>2</sub> ocean pH rises, reflecting loss of carbon from the**  
29 **ocean to the atmosphere. Correspondingly, at shallower sites we find**  
30 **rapid (millennial to centennial-scale) pH decreases during abrupt CO<sub>2</sub>**  
31 **rise, reflecting the rapid transfer of carbon from the deep to the upper**

32 **ocean and atmosphere. These data thus confirm the importance of the**  
33 **deep Southern Ocean in ice age CO<sub>2</sub> change, and demonstrate that deep**  
34 **ocean CO<sub>2</sub> release can occur as a dynamic feedback to rapid climate**  
35 **change on centennial timescales.**

36

37

38 The Southern Ocean may act as a net source of CO<sub>2</sub> from the deep ocean to  
39 the atmosphere or a net sink <sup>3</sup>, depending on the balance between regional  
40 CO<sub>2</sub>-supply via circulation and CO<sub>2</sub>-removal via biological productivity.  
41 Various records have shown that large changes in circulation <sup>4,5</sup> and biological  
42 productivity <sup>6</sup> occurred in the Southern Ocean on glacial timescales, with the  
43 potential to change the partitioning of carbon between the deep ocean and the  
44 atmosphere. However, reconstructions of deep ocean CO<sub>2</sub> storage are  
45 currently sparse and more complex. For instance records of CO<sub>2</sub> chemistry  
46 from the deep Atlantic <sup>7</sup> and deep Pacific <sup>8</sup> show decreases in carbonate ion  
47 saturation and pH during millennial-scale intervals of atmospheric CO<sub>2</sub> rise; in  
48 the absence of other processes, low carbonate ion and pH imply an increase  
49 in CO<sub>2</sub>-storage in the deep ocean, so these signals are thought instead to be  
50 dominated by changes in circulation and deep water masses. On longer  
51 timescales, records from the deep Indo-Pacific <sup>9</sup> appear to reflect changes in  
52 CO<sub>2</sub>-storage, but are damped by the buffering influence of carbonate  
53 compensation. Records of deep ocean CO<sub>2</sub> chemistry that clearly  
54 demonstrate CO<sub>2</sub> storage during atmospheric CO<sub>2</sub> fall, and CO<sub>2</sub> release  
55 during atmospheric CO<sub>2</sub> rise, have proved elusive.

56

57 Here we test the hypothesis that carbon storage in the deep Southern Ocean  
58 played a key role in ice age CO<sub>2</sub> change, with new boron isotope ( $\delta^{11}\text{B}$ ) data  
59 from uranium-thorium dated deep-sea corals from the Drake Passage (Figure  
60 1; Methods)<sup>4</sup>. The boron isotope pH proxy (see Methods) provides a sensitive  
61 measure of the ocean carbonate system, closely tracking CO<sub>2</sub> concentrations  
62 and reflecting the ratio of the two master variables, dissolved inorganic carbon  
63 (DIC) and alkalinity. Although full reconstruction of the carbonate system

64 requires knowledge of a second parameter, it is unlikely that alkalinity was  
65 lower in the glacial ocean <sup>10</sup>, or varied as dynamically as DIC, so our  $\delta^{11}\text{B}$ -pH  
66 record may be largely attributed to changes in carbon storage. Note that as  
67 our  $\delta^{11}\text{B}$  record extends beyond the pH calibration possible in modern *D.*  
68 *dianthus* (Figure S5) we focus our discussion on relative changes in pH as  
69 traced by coral  $\delta^{11}\text{B}$ , and provide absolute pH estimates in Figure S1 for  
70 reference. Our sample sites reflect distinct volumes of the deep ocean <sup>11</sup>: the  
71 “lower cell” sites lie close to the Antarctic continental margin, bathed by  
72 waters that plumb the mid to lower depths of the deep ocean; the “upper cell”  
73 sites lie on lighter isopycnal surfaces, bathed by waters found at shallower  
74 depths in the ocean basins (Figure 1).

75

76 During the LGM and early deglaciation we see a clear gradient between the  
77 lower cell sites, which show low  $\delta^{11}\text{B}$  and pH, and upper cell sites, with  
78 relatively high  $\delta^{11}\text{B}$  and pH (Figure 2). This supports the idea that during  
79 glacial intervals the deep ocean – and its carbon – was more stratified into  
80 two cells with limited interaction <sup>11</sup>. Our data show that the lower cell was rich  
81 in carbon compared to the upper cell and compared to modern values  
82 expected at this site (Figure 1, S1), providing strong support for the  
83 hypothesis that the deep glacial ocean sequestered carbon from the upper  
84 ocean and the atmosphere <sup>2</sup>.

85

86 During the deglaciation this gradient in deep carbon breaks down, with lower  
87 cell pH rising in step with atmospheric  $\text{CO}_2$ , and pH in the upper cell falling  
88 towards lower cell values (Figure 3). This provides direct evidence for the  
89 transfer of carbon from the deep ocean to the upper ocean and the  
90 atmosphere. Carbon transfer to the upper ocean appears particularly  
91 pronounced at ~14.7 and ~11.7 ka, coincident with the centennial-scale jumps  
92 in atmospheric  $\text{CO}_2$  <sup>12</sup> associated with abrupt warming in the Northern  
93 Hemisphere. This provides the first evidence of a fast teleconnection  
94 between abrupt changes in the North Atlantic and the carbon chemistry of the  
95 deep Southern Ocean. Lower cell *D. dianthus* samples have not been found

96 in the Holocene (see Methods), but the available data at the end of the  
97 deglaciation and in the modern water column suggest much weaker pH  
98 gradients, consistent with less-pronounced property gradients in the modern  
99 deep ocean compared to the glacial <sup>11,13,14</sup>.

100

101 Our data show that the carbonate chemistry of the deep Southern Ocean was  
102 closely linked to atmospheric CO<sub>2</sub> change over the last 40 ka. These data  
103 thus provide a crucial missing piece of the glacial CO<sub>2</sub> puzzle: the most direct  
104 evidence to date of deep Southern Ocean carbon storage and release, as  
105 previously inferred from physical properties <sup>5,13</sup>, carbon isotopes <sup>15</sup>, and  
106 oxygen content <sup>16</sup> (Figure 2 & S3). While other processes <sup>3</sup> and regions <sup>8</sup> may  
107 contribute to the full magnitude of glacial-interglacial CO<sub>2</sub> change, our data  
108 demonstrate a key role for the Southern Ocean on millennial to centennial  
109 timescales.

110

111 Several processes may contribute to the changes in CO<sub>2</sub> storage observed in  
112 our record, including changes in ventilation <sup>4,16</sup>, biological pump efficiency <sup>6</sup>,  
113 and sea ice <sup>17</sup> (Figure S3). We note a close correspondence between lower  
114 cell pH and ice core sea salt sodium, a proxy that may reflect changes in sea  
115 ice production <sup>18 19</sup> (Figure 2), suggesting that sea ice may play an important  
116 role in CO<sub>2</sub> change. Sea ice has the potential to influence CO<sub>2</sub> storage both  
117 through its influence as a “lid” on surface-ocean outgassing <sup>17</sup>, and its impact  
118 on deep circulation <sup>11</sup>. Expansion of sea ice at the LGM <sup>11</sup>, alongside an  
119 increase in surface ocean density in the Southern Ocean relative to the North  
120 Atlantic <sup>20</sup>, would help create an expanded lower cell with salty <sup>13</sup>, CO<sub>2</sub>-rich  
121 water. This may shoal the upper/lower cell boundary above the zone of  
122 enhanced mixing over rough bottom topography <sup>11,14</sup>, trapping salt and CO<sub>2</sub> in  
123 the abyss. Accumulation of CO<sub>2</sub> at depth would be further promoted by an  
124 enhanced biological pump due to iron fertilization <sup>6</sup> and increased upper  
125 ocean stratification, which would also reduce CO<sub>2</sub> escape through leads and  
126 during ice-free conditions.

127

128 This framework may also explain release of CO<sub>2</sub> from the deep Southern  
129 Ocean on millennial timescales<sup>21</sup>. CO<sub>2</sub> rise typically occurs during intervals  
130 of cold stadial conditions in the Northern Hemisphere and warming in the  
131 South (the bipolar seesaw)<sup>22</sup>. This southern warming is associated with a  
132 decrease in Southern sea ice (Figures 2, 3) and a decrease in the Southern  
133 Ocean to North Atlantic surface density gradient, shifting the boundary  
134 between the overturning cells to greater depth in the basins<sup>11 20</sup>. CO<sub>2</sub>-rich  
135 water previously isolated in the abyss may thus be mixed into the upper cell  
136 over rough topography in the ocean basins, and/or transferred into the upper  
137 cell upon upwelling North of the sea ice edge, perhaps aided by the westerly  
138 winds<sup>23,24</sup> or increased mixed layer depths in the Southern Ocean. CO<sub>2</sub> loss  
139 from the deep ocean may also aided by reduced biological pump efficiency<sup>6</sup>.  
140 Whatever the exact mechanism, this carbon transfer is recorded by a pH  
141 increase in our lower cell corals and a pH decrease in our upper cell corals,  
142 as CO<sub>2</sub> is transferred to the upper ocean and the atmosphere. Note that as a  
143 southward shift in the fronts at these times might be expected to expose our  
144 sites to higher-pH water (Figure 1), the transfer of low-pH DIC-rich water into  
145 the upper cell may be even larger than observed. Indeed a southward frontal  
146 shift and breakdown in stratification likely explain the younging seen in upper  
147 cell radiocarbon<sup>4,25</sup> at this time (Figure S4). Upwelling of carbon and nutrient-  
148 rich water during cold Northern Hemisphere stadials is also supported by low  
149 pH in surface waters, as recorded by boron isotopes in planktic foraminifera  
150<sup>26</sup>, and enhanced opal fluxes<sup>23</sup> (Figure 3 & S4). If salt from the high salinity  
151 lower cell<sup>13</sup> is also transferred back into the upper cell, this may aid the re-  
152 initiation of NADW formation<sup>27</sup>. Once interstadial conditions are  
153 reestablished in the North Atlantic, the Southern Ocean starts to cool via the  
154 bipolar seesaw and sea ice expands<sup>28</sup>. This shoals the cell boundary,  
155 reduces ocean-atmosphere exchange, and allows CO<sub>2</sub> and salt to again  
156 become trapped in the abyss (Figure 4).

157

158 The centennial-scale CO<sub>2</sub> jumps at 14.7 and 11.7 ka<sup>12</sup>, which are associated  
159 with pronounced minima in upper cell pH (Figure 3), appear to require a more  
160 efficient mode of Southern Ocean CO<sub>2</sub> release associated with abrupt

161 Northern Hemisphere warming <sup>25</sup>. High-resolution records of Antarctic  
162 deuterium excess indicate a northward shift in the Southern Westerly winds  
163 synchronous with abrupt Northern Hemisphere warming <sup>29</sup>; in contrast the  
164 bipolar seesaw cooling response in the south is lagged, with Antarctic  $\delta^{18}\text{O}$   
165 and sea salt sodium taking around 200 years to show the onset of cooling  
166 conditions and increased sea ice production <sup>28</sup> (Figure 3). This may lead to a  
167 transient condition in the Southern Ocean where  $\text{CO}_2$  can be efficiently mixed  
168 up from the lower cell <sup>24</sup>, due to the fast shift in the winds, and then outgas  
169 unimpeded by sea ice, which has not yet expanded <sup>17</sup>. The northward shift in  
170 the fronts might also contribute to the pH minima by exposing our upper cell  
171 sites to lower-pH water from the South (Figure 1), but such a shift would have  
172 to be large given that upper cell pH appears to reach values similar to, or  
173 even lower than, the lower cell at this time, suggesting increased input of  $\text{CO}_2$ -  
174 rich water is required. Increased input of previously isolated carbon-rich  
175 waters is also seen in radiocarbon data <sup>4,25</sup>, which show an interruption of  
176 their deglacial younging and a slight increase in age during these events  
177 (Figure S4). Whatever the exact mechanisms involved, our data demonstrate  
178 that the Southern Ocean may fill with  $\text{CO}_2$ -rich waters on centennial  
179 timescales and may thus give out its carbon rapidly, countering suggestions  
180 that centennial-scale  $\text{CO}_2$  jumps are too quick for a deep ocean driver and  
181 require exogenous carbon addition (such as from methane hydrates or the  
182 terrestrial biosphere <sup>30</sup>). Our data show that rapid changes in the Southern  
183 Ocean acted in concert with strong AMOC resumption <sup>25</sup> to drive rapid  $\text{CO}_2$   
184 rise.

185

186 Although our lower cell  $\delta^{11}\text{B}$ -pH data generally show a close coupling with  
187 atmospheric  $\text{CO}_2$ , this relationship is somewhat muted during peak glacial  
188 conditions, with pronounced minima in pH at ~26 and 20 ka, alongside  
189 extensive sea ice <sup>28</sup>, low upwelling <sup>23</sup>, and an efficient biological pump <sup>6</sup>  
190 (Figure S3), but minimal change in atmospheric  $\text{CO}_2$ . This supports the idea  
191 of a lower limit on atmospheric  $\text{CO}_2$  at ~190 ppm <sup>31</sup>: although Southern Ocean  
192 carbon storage continues to increase, its influence on the atmosphere

193 appears to be offset by other processes, perhaps the onset of CO<sub>2</sub> limitation  
194 on primary productivity on land <sup>31</sup>.

195

196 Overall, our data provide a clear demonstration that storage and release of  
197 CO<sub>2</sub> in the deep Southern Ocean plays a central role in glacial-interglacial  
198 atmospheric CO<sub>2</sub> change. These changes in ocean CO<sub>2</sub> storage were likely  
199 driven by a combination of changes in ocean circulation, biological pump  
200 efficiency, and sea ice cover. We note a close correspondence between CO<sub>2</sub>  
201 storage and ice core sea ice sodium records, which may suggest that  
202 Southern Ocean sea ice plays a key role, due to its joint influence on deep  
203 overturning and surface outgassing. This provides a mechanistic explanation  
204 for the tight link between Antarctic temperature and CO<sub>2</sub> change on glacial-  
205 interglacial timescales, though several processes acting together are likely  
206 required to explain the full magnitude of glacial CO<sub>2</sub> change. Our data also  
207 highlight the ability of the Southern Ocean – and its CO<sub>2</sub> – to respond to  
208 millennial and centennial-scale shifts in climate linked to the North Atlantic’s  
209 overturning circulation. Indeed, it is possible that the framework presented  
210 here, which links the storage and release of deep ocean CO<sub>2</sub> and salt to  
211 changes in Southern Ocean sea ice and the bipolar seesaw, may help  
212 account for the occurrence of millennial-scale CO<sub>2</sub> and climate change during  
213 mid-glacial conditions. At these times, moderate sea ice extent means that  
214 the boundary between the ocean’s lower and upper cells is located near the  
215 top of rough seafloor topography. Small shifts in the cell boundary, linked to  
216 changes in the Southern sea ice edge, may thus drive large shifts in the  
217 degree of mixing between the lower and upper cells, and their salt and CO<sub>2</sub>.  
218 This framework may also give behavior similar to “density oscillator” models  
219 for rapid climate change <sup>27,32,33</sup>: when AMOC is active and the Northern  
220 Hemisphere warms, the South cools and sea ice expands, progressively  
221 isolating cold salty water (and CO<sub>2</sub>) in the lower cell. This may make the  
222 AMOC vulnerable to collapse, at which point the South warms, sea ice  
223 retreats, and the cell-boundary deepens. This helps mix salt (and CO<sub>2</sub>) back  
224 into the upper cell and makes the lower cell fresher and warmer, reducing the

225 deep ocean density contrast, and helping poise the system for AMOC  
226 resumption.

227



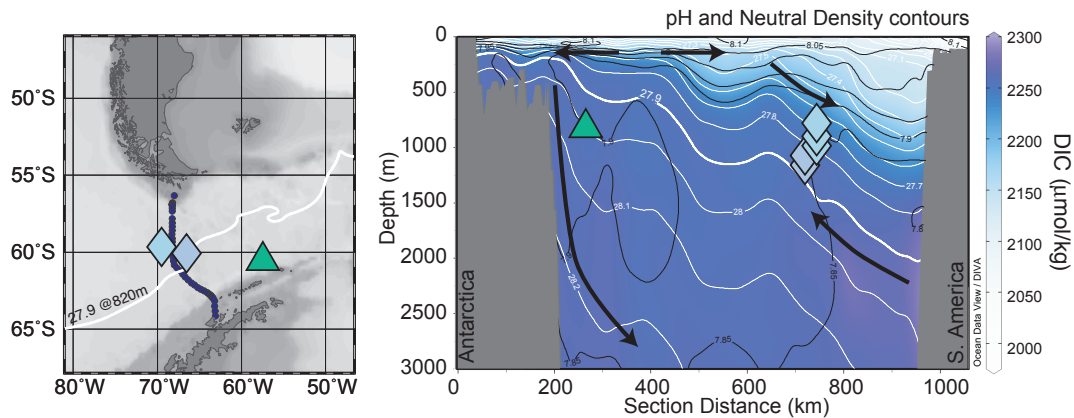
## 228 References

229

- 230 1. Broecker, W. S. Glacial to interglacial changes in ocean chemistry.  
231 *Progress in Oceanography* **11**, 151–197 (1982).
- 232 2. Sarmiento, J. L. & Toggweiler, J. R. A new model for the role of the  
233 oceans in determining atmospheric pCO<sub>2</sub>. *Nature* **308**, 621–624 (1984).
- 234 3. Sigman, D. M., Hain, M. P. & Haug, G. H. The polar ocean and glacial  
235 cycles in atmospheric CO<sub>2</sub> concentration. *Nature* **466**, 47–55 (2010).
- 236 4. Burke, A. & Robinson, L. F. The Southern Ocean's Role in Carbon  
237 Exchange During the Last Deglaciation. *Science* **335**, 557–561 (2012).
- 238 5. Roberts, J. *et al.* Evolution of South Atlantic density and chemical  
239 stratification across the last deglaciation. *PNAS* 201511252–14 (2016).  
240 doi:10.1073/pnas.1511252113
- 241 6. Martinez-Garcia, A. *et al.* Iron Fertilization of the Subantarctic Ocean  
242 During the Last Ice Age. *Science* **343**, 1347–1350 (2014).
- 243 7. Yu, J. *et al.* Deep South Atlantic carbonate chemistry and increased  
244 interocean deep water exchange during last deglaciation. *Quaternary*  
245 *Science Reviews* **90**, 80–89 (2014).
- 246 8. Rae, J. W. B. *et al.* Deep water formation in the North Pacific and  
247 deglacial CO<sub>2</sub> rise. *Paleoceanography* **29**, 645–667 (2014).
- 248 9. Yu, J. *et al.* Responses of the deep ocean carbonate system to carbon  
249 reorganization during the Last Glacial–interglacial cycle. *Quaternary*  
250 *Science Reviews* **76**, 39–52 (2013).
- 251 10. Rickaby, R. E. M., Elderfield, H., Roberts, N., Hillenbrand, C. D. &  
252 Mackensen, A. Evidence for elevated alkalinity in the glacial Southern  
253 Ocean. *Paleoceanography* **25**, PA1209 (2010).
- 254 11. Ferrari, R. *et al.* Antarctic sea ice control on ocean circulation in present  
255 and glacial climates. *PNAS* **111**, 8753–8758 (2014).
- 256 12. Marcott, S. A. *et al.* Centennial-scale changes in the global carbon cycle  
257 during the last deglaciation. **514**, 616–619 (2014).
- 258 13. Adkins, J. F., McIntyre, K. & Schrag, D. P. The salinity, temperature,  
259 and δ<sup>18</sup>O of the glacial deep ocean. *Science* **298**, 1769–1773 (2002).
- 260 14. Burke, A., Stewart, A. L., Adkins, J. F. & Ferrari, R. The glacial mid-  
261 depth radiocarbon bulge and its implications for the overturning  
262 circulation. *Paleoceanography* **30**, 1021–1039 (2015).
- 263 15. Charles, C. D. *et al.* Millennial scale evolution of the Southern Ocean  
264 chemical divide. *Quaternary Science Reviews* **29**, 399–409 (2010).
- 265 16. Jaccard, S. L., Galbraith, E. D., Martinez-Garcia, A. & Anderson, R. F.  
266 Covariation of deep Southern Ocean oxygenation and atmospheric CO<sub>2</sub>  
267 through the last ice age. *Nature* **530**, 207–210 (2016).
- 268 17. Stephens, B. B. & Keeling, R. F. The influence of Antarctic sea ice on  
269 glacial-interglacial CO<sub>2</sub> variations. *Nature* **404**, 171–174 (2000).
- 270 18. Wolff, E. W. *et al.* Southern Ocean sea-ice extent, productivity and iron  
271 flux over the past eight glacial cycles. *Nature* **440**, 491–496 (2006).
- 272 19. Abram, N. J., Wolff, E. W. & Curran, M. A. J. A review of sea ice proxy  
273 information from polar ice cores. *Quaternary Science Reviews* **79**, 168–  
274 183 (2013).
- 275 20. Galbraith, E. & de Lavergne, C. Response of a comprehensive climate

- 276 model to a broad range of external forcings: relevance for deep ocean  
277 ventilation and the development of late Cenozoic ice ages. *Climate*  
278 *Dynamics* 1–27 (2018). doi:10.1007/s00382-018-4157-8
- 279 21. Ahn, J. & Brook, E. J. Atmospheric CO<sub>2</sub> and Climate on Millennial Time  
280 Scales During the Last Glacial Period. *Science* **322**, 83–85 (2008).
- 281 22. Stocker, T. F. The seesaw effect. *Science* (1998).
- 282 23. Anderson, R. F. *et al.* Wind-Driven Upwelling in the Southern Ocean  
283 and the Deglacial Rise in Atmospheric CO<sub>2</sub>. *Science* **323**, 1443–1448  
284 (2009).
- 285 24. Abernathy, R. & Ferreira, D. Southern Ocean isopycnal mixing and  
286 ventilation changes driven by winds. *Geophysical Research Letters* **42**,  
287 10,357–10,365 (2015).
- 288 25. Chen, T. *et al.* Synchronous centennial abrupt events in the ocean and  
289 atmosphere during the last deglaciation. *Science* **349**, 1537–1541  
290 (2015).
- 291 26. Martínez-Botí, M. A. *et al.* Boron isotope evidence for oceanic carbon  
292 dioxide leakage during the last deglaciation. *Nature* **518**, 219–222  
293 (2015).
- 294 27. Broecker, W. S., Bond, G., Klas, M., Bonani, G. & Wolfli, W. A salt  
295 oscillator in the glacial Atlantic? 1. The concept. *Paleoceanography* **5**,  
296 469–477 (1990).
- 297 28. Members, W. D. P. *et al.* Precise inter-polar phasing of abrupt climate  
298 change during the last ice age. *Nature Publishing Group* **520**, 661–16  
299 (2015).
- 300 29. Markle, B. R. *et al.* Global atmospheric teleconnections during  
301 Dansgaard-Oeschger events. *Nature Geoscience* **10**, 36–40 (2017).
- 302 30. Köhler, P., Knorr, G. & Bard, E. Permafrost thawing as a possible  
303 source of abrupt carbon release at the onset of the Bølling/Allerød.  
304 *Nature Communications* **5**, 1–10 (2014).
- 305 31. Galbraith, E. D. & Eggleston, S. A lower limit to atmospheric CO<sub>2</sub>  
306 concentrations over the past 800,000 years. *Nature Geosci* **10**, 295–  
307 298 (2017).
- 308 32. Bereiter, B., Shackleton, S., Baggenstos, D., Kawamura, K. &  
309 Severinghaus, J. Mean global ocean temperatures during the last  
310 glacial transition. *Nature Publishing Group* **553**, 39–44 (2018).
- 311 33. Keeling, R. F. & Stephens, B. B. Antarctic sea ice and the control of  
312 Pleistocene climate instability. *Paleoceanography* (2001).
- 313

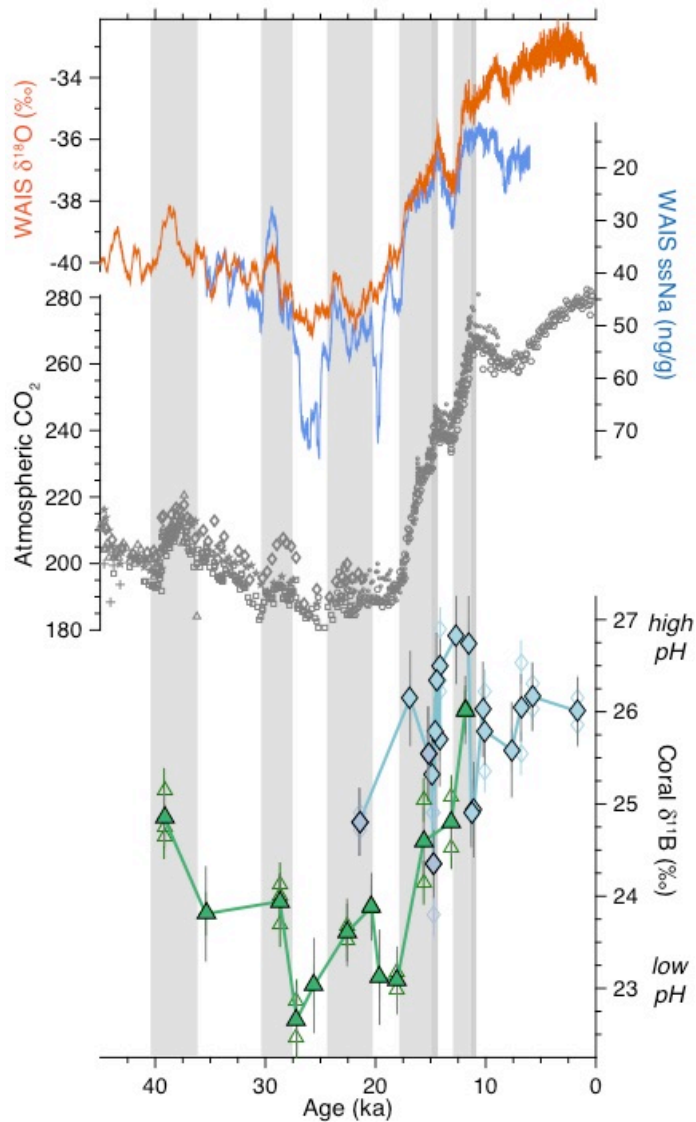
314



315

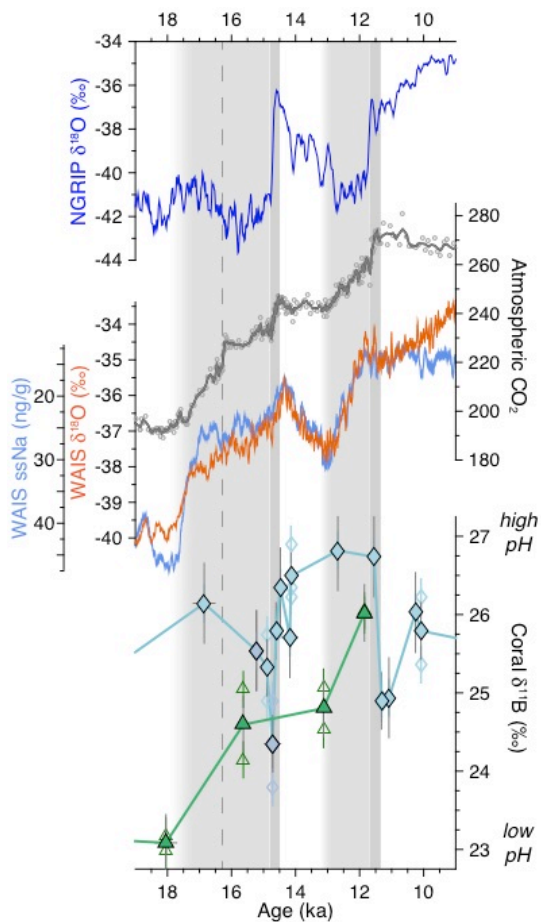
316 **Figure 1: Locations of deep-sea coral samples.** The cross section (right  
317 panel) is constructed from hydrographic stations across the Drake Passage  
318 (dark blue dots on map, left panel). Steeply dipping isopycnals in this region  
319 (white contours) mean our sites fall into two groups spanning distinct volumes  
320 of the deep ocean <sup>11</sup>. The green triangle marks the lower cell sites, which lie  
321 close to the Antarctic continental margin in the Shackleton Fracture Zone; the  
322 blue diamonds the upper cell sites, which lie at lower densities on the Sars  
323 (lighter blue) and Interim (darker blue) seamounts. Lower cell waters are rich  
324 in DIC (shading, right panel) with low pH (black contours); upper cell waters  
325 have higher pH and are more closely connected to the atmosphere. Coral  
326 locations on the section are given in coordinates of depth and neutral density,  
327 based on CTD data collected alongside the coral dredges. Note that there is  
328 no significant offset in our  $\delta^{11}\text{B}$  data between upper cell corals from different  
329 depths (Figure S2), and that differences in pH between these sites are small  
330 compared to the range seen in our records. The 27.9 neutral density contour  
331 in the map view (left) is shown at 820 m, the average depth of our corals.  
332 Section data are from GLODAPv2 <sup>34,35</sup>, plotted using isopycnal gridding in  
333 Ocean Data View.

334



335

336 **Figure 2: Deep Southern Ocean  $\text{CO}_2$  chemistry, atmospheric  $\text{CO}_2$ , and**  
 337 **Antarctic climate records over the last 40,000 years.** Green triangles and  
 338 blue diamonds show lower and upper cell deep-sea coral  $\delta^{11}\text{B}$  data  
 339 respectively. Individual subsamples are shown in small open symbols and  
 340 mean values in larger filled symbols. Error bars on individual subsamples are  
 341 equivalent to 2 SD analytical reproducibility and error bars on mean coral  
 342 values represent 2 SE uncertainty on the mean of replicate subsamples (see  
 343 Methods). Synchronised ice core  $\text{CO}_2$  data<sup>36</sup> are shown in grey symbols:  
 344 circles from Dome C, dots from WAIS, stars from Taylor Dome, triangles from  
 345 TALDICE, pluses from EDML, diamonds from Byrd, and squares from Siple  
 346 Dome. WAIS  $\delta^{18}\text{O}$  (orange line), which reflects Antarctic temperature, and  
 347 sea salt sodium (blue line), a proxy for sea ice, have been smoothed with a  
 348 running mean<sup>28</sup>. Grey bands highlight intervals of  $\text{CO}_2$  rise.



350

351 **Figure 3: Deglacial records of deep Southern Ocean CO<sub>2</sub> chemistry,**  
 352 **atmospheric CO<sub>2</sub>, and climate over Antarctica and Greenland.** Green  
 353 green triangles and blue diamonds show lower and upper cell deep-sea coral δ<sup>11</sup>B  
 354 data respectively. Individual subsamples are shown in small open symbols  
 355 and mean values in larger filled symbols. Error bars on individual subsamples  
 356 are equivalent to 2 SD analytical reproducibility and error bars on mean coral  
 357 values represent 2 SE uncertainty on the mean of replicate subsamples (see  
 358 Methods). Greenland ice core δ<sup>18</sup>O (dark blue line), WAIS δ<sup>18</sup>O (orange line),  
 359 and sea salt sodium (blue line), have been smoothed with a running mean<sup>28</sup>.  
 360 CO<sub>2</sub> data (grey symbols) are from WAIS<sup>12</sup> with a 5-point running mean (grey  
 361 line). Light grey vertical bands highlight intervals of millennial-scale CO<sub>2</sub> rise;  
 362 dark grey vertical bands highlight intervals of centennial-scale CO<sub>2</sub> rise  
 363 associated with North Hemisphere warming, and the vertical dashed line  
 364 indicates the rapid CO<sub>2</sub> rise event that occurs at 16.3 ka, within Heinrich  
 365 Stadial 1.

366

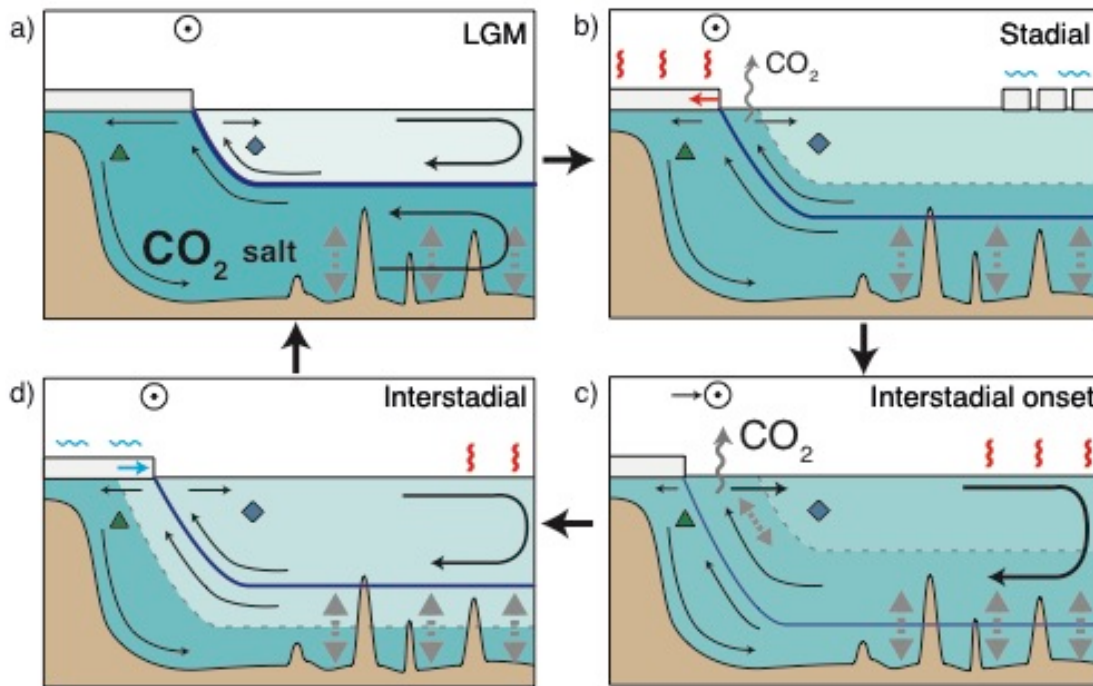


**Figure 4**

a) At the LGM extensive Southern Ocean sea ice creates an expanded lower cell with salty, CO<sub>2</sub>-rich water. The cell boundary is shoaled above the zone of enhanced mixing over rough bottom topography, isolating salt and CO<sub>2</sub> in the abyss.

b) During a Northern Hemisphere stadial event, North Atlantic overturning is reduced, the Southern Ocean warms, and sea ice retreats. This shifts the cell boundary such that water previously isolated in the lower cell now upwells North of the sea ice edge. This water – and its CO<sub>2</sub> and salt – are transferred to the upper ocean and CO<sub>2</sub> outgases to the atmosphere. Transfer of salt from the lower to the upper cell may help re-initiate NADW formation.

c) At the onset of a Northern Hemisphere interstadial event (e.g. Bølling-Allerød, end Younger Dryas), resumption of NADW warms the Northern Hemisphere and leads to a rapid Northward shift in the Westerly winds; the Southern Ocean temperature and sea ice response is slower. This creates a transient condition where sea ice is unable to shield the ocean from enhanced isopycnal mixing nor the atmosphere from enhanced outgassing, leading to centennial-scale CO<sub>2</sub> rise.

d) As the interstadial continues, the Southern Ocean cools and sea ice expands. This shoals the cell boundary and allows salt and carbon to again become trapped in the abyss.

Climate states with moderate sea ice extent, where the cell boundary hovers around the top of rough seafloor topography, may give favourable conditions for rapid climate and CO<sub>2</sub> change, as the ocean flips between modes of connection vs isolation of the upper and lower cells.

398 **Acknowledgements**

399 This work was supported by NERC Standard Grant NE/N003861/1 to  
400 J.W.B.R. and L.F.R., a NOAA Climate and Global Change VSP Fellowship to  
401 J.W.B.R., NERC Standard Grant NE/M004619/1 to AB and JWBR, a NERC  
402 Strategic Environmental Science Capital Grant to A.B. and J.W.B.R., Marie  
403 Curie Career Integration Grant CIG14-631752 to AB, an ERC consolidator  
404 grant to L.F.R., NSF grant OCE-1503129 to J.F.A., and NERC studentships to  
405 B.T. and E.L. We thank 3 anonymous reviewers for comments that  
406 substantially improved this manuscript.

407

408 **Author Contributions**

409 J.W.B.R., A.B., and L.F.R. designed the study. A.B., L.F.R., T.C., and T.L.  
410 collected and uranium-thorium dated the coral samples. J.W.B.R., B.T., E.L.,  
411 C.C., J.S., and D.C.N. made boron isotope analyses. All authors contributed  
412 to the interpretation and the preparation of the manuscript.

413

414 The authors declare no competing interests.

415 Correspondence and requests for materials should be addressed to J.W.B.R  
416 ([jwbr@st-andrews.ac.uk](mailto:jwbr@st-andrews.ac.uk))

417

## 418 Methods

419

### 420 **Sample collection and chronology**

421 Deep-sea coral samples were collected by dredge during two cruises in the  
422 Drake Passage (NBP0805 and NBP1103). A total of 392 *D. dianthus*  
423 samples were initially “reconnaissance” dated, either by  $^{14}\text{C}$  <sup>37,38</sup> or laser  
424 ablation U-Th <sup>25,39</sup>, to obtain preliminary ages. Suitable samples with ages  
425 within the last ~50 ka were then precisely dated by isotope dilution U-Th by  
426 MC-ICPMS <sup>4,25</sup>. All ages have been published previously, and have typical  
427 uncertainties of around  $\pm 1\%$  (2 SD), though this varies between samples  
428 depending on their initial  $^{230}\text{Th}$  (calculated from measured  $^{232}\text{Th}$  and assuming  
429 an initial atomic  $^{232}\text{Th}/^{230}\text{Th}$  ratio of  $12,500 \pm 12,500$ ). Age errors are plotted  
430 in all time series figures but are typically smaller than the symbols. This  
431 precisely-dated and unbioturbated deep sea archive provides a unique record  
432 of ocean pH change at resolution comparable to the ice cores.

433

### 434 **Sample preparation**

435 Coral pieces were sampled from the growing tip of coral septa. Samples were  
436 physically cleaned using a Dremmel tool to remove all visible iron-manganese  
437 oxides and any chalky white carbonate, indicative of alteration.

438 We tested the potential influence of microstructural variability on coral  $\delta^{11}\text{B}$   
439 with multiple solid sub-samples from the same coral (Figure S6). Coral  
440 centres of calcification have previously been observed to have anomalously  
441 light boron isotope values, along with high Mg/Ca and low U/Ca <sup>40-44</sup>, and we  
442 observe this same coupled variability in our coral subsamples (Figure S6).  
443 However this microstructural signal is typically small compared to the size of  
444 the boron isotope signals seen in our record. We had expected the smaller  
445 subsamples to exhibit more scatter, due to the potential influence of coral  
446 centers of calcification (COCs), but this is not shown in these data. There is  
447 in fact slightly more variability between larger chunks, perhaps due to the  
448 increased chance of sampling some COC material. For our records we used



449 coral pieces of ~1 mg. We also mitigated microstructural influences by taking  
450 multiple solid subsamples from each coral when possible (shown as open  
451 symbols). Two subsamples (at 1.6 ka and 20.4 ka) were rejected from our  
452 total set of 55 as having anomalous  $\delta^{11}\text{B}$  values (~1 ‰ lighter than the mean  
453 of 3-4 other subsamples from that coral), which may be due to the impact of  
454 COC material.

455

#### 456 **Boron isotope analysis**

457 Solid coral samples were crushed to a grain size <1 mm using an agate pestle  
458 and mortar. Samples were then subjected to oxidative cleaning to remove  
459 organic matter following established protocols<sup>45-48</sup>, using warm 1 % hydrogen  
460 peroxide, buffered in 0.1 M  $\text{NH}_4\text{OH}$ , followed by leaching in 0.0001 M  $\text{HNO}_3$ ,  
461 and dissolution in 0.075 M distilled  $\text{HNO}_3$ . Boron was purified from the  
462 sample matrix using column chromatography with the boron-specific ion  
463 exchange resin Amberlite 743<sup>49-51</sup>.

464 Boron isotope composition was analysed by MC-ICPMS by sample-standard  
465 bracketing<sup>47,48,51</sup>. Early analyses used  $\text{NH}_3$  to improve boron washout in the  
466 spray chamber<sup>52</sup>, which reduces background signals to ~3 % of the  
467 preceding sample within ~3 minutes<sup>51</sup>. More recent analyses used dilute HF  
468<sup>53</sup>, which reduces background signals to ~0.5 % within ~3 minutes. In  
469 contrast to some previous work, where samples are analysed in pure 0.3 M  
470 HF<sup>53</sup>, we add a small volume of concentrated HF to our sample following  
471 column elution in 0.5 M  $\text{HNO}_3$ , giving a solution of 0.5 M  $\text{HNO}_3$  + 0.3 M HF.  
472 Similarly, bracketing standards (NIST 951) and instrument blank acid were  
473 analysed in 0.5 M  $\text{HNO}_3$  + 0.3 M HF to ensure consistent mass bias and blank  
474 corrections, though beyond improved washout we do not find any significant  
475 influence of HF concentration: boric acid standards run as dummy-samples  
476 run with HF concentrations from 0 to 0.5 M HF bracketed against 951 in 0.5 M  
477  $\text{HNO}_3$  + 0.3 M HF all yield identical boron isotope ratios. Carbonate  
478 standards (JCP, NIST RM8301C) passed through columns and run with  $\text{NH}_3$   
479 or HF also yield identical values.

480 All preparation and analytical work was carried out in boron-free clean  
481 laboratory conditions. Over the course of this work samples were analysed at  
482 the University of Bristol and Caltech on a Neptune MC-ICPMS, and the  
483 University of St Andrews on a Neptune Plus MC-ICPMS, though in all cases  
484 following nearly identical protocols. Each of these laboratories has taken part  
485 in published and ongoing inter-laboratory comparison studies <sup>48</sup> and there is  
486 no analytical offset between samples run in these laboratories.

487 Long-term analytical reproducibility on  $\delta^{11}\text{B}$  measurements in these  
488 laboratories (assessed with carbonate standards given the same treatment as  
489 samples) is around 0.23 ‰ (2 SD) on samples of the size used here (~20 ng  
490 boron) – this is the error bar given on individual subsamples (open symbols in  
491 figures). We use a more conservative uncertainty for our mean coral  $\delta^{11}\text{B}$   
492 values (filled symbols in figures), to account for the  $\delta^{11}\text{B}$  variability between  
493 subsamples from the same coral. This is based on the pooled standard  
494 deviation of the replicate samples in our records and in Figure S6 (2 SD =  
495 0.51 ‰). Uncertainty is reduced on mean values with multiple replicates ( $n$ ),  
496 which is accounted for using the standard error ( $\text{SD}/\sqrt{n}$ ).

497

#### 498 $\delta^{11}\text{B}$ and pH in deep-sea corals

499 The boron isotope pH proxy provides a sensitive measure of the ocean  
500 carbonate system, though in common with many proxies, is also influenced by  
501 modification during biomineralisation <sup>54-57</sup>. In particular, coral  $\delta^{11}\text{B}$  is  
502 influenced by internal pH-elevation during biomineralisation <sup>58,59</sup>, which may  
503 buffer its sensitivity to external seawater pH changes in some settings. To  
504 examine this we have compiled modern *D. dianthus*  $\delta^{11}\text{B}$  calibration data  
505 <sup>44,56,60</sup> from water depths >100 m, and have added two recent Southern  
506 Ocean samples. This indicates that the relationship between seawater pH  
507 and coral  $\delta^{11}\text{B}$  is curved, with  $\delta^{11}\text{B}$  becoming more sensitive to external  
508 seawater at lower pH (Figure S5). This suggests that corals find it harder to  
509 elevate internal pH as external conditions become more acidic, which is  
510 reasonable, given the increase in energy demand required for additional  
511 proton expulsion <sup>61</sup>. It also means that corals are likely to be more sensitive to

512 external pH conditions at lower pH sites, such as the Southern Ocean  
513 locations in this study. Hence, the pH changes that occurred during the last  
514 40,000 yr are evident as large, easily resolvable changes in  $\delta^{11}\text{B}$  in our coral  
515 record.

516 Reconstructed pH based on this calibration is shown in Figure S1. Given the  
517 paucity of modern deep-sea coral samples from low-pH waters, our record  
518 extends beyond the available calibration range. As a result conversion to  
519 absolute pH values carries relatively large uncertainty, which is hard to  
520 assess. We thus prefer to focus on relative changes in the  $\delta^{11}\text{B}$  records  
521 themselves, which provide a proxy of carbonate chemistry in their own right<sup>62</sup>,  
522 analogous to the typical use of  $\delta^{18}\text{O}$  records in paleoceanography.

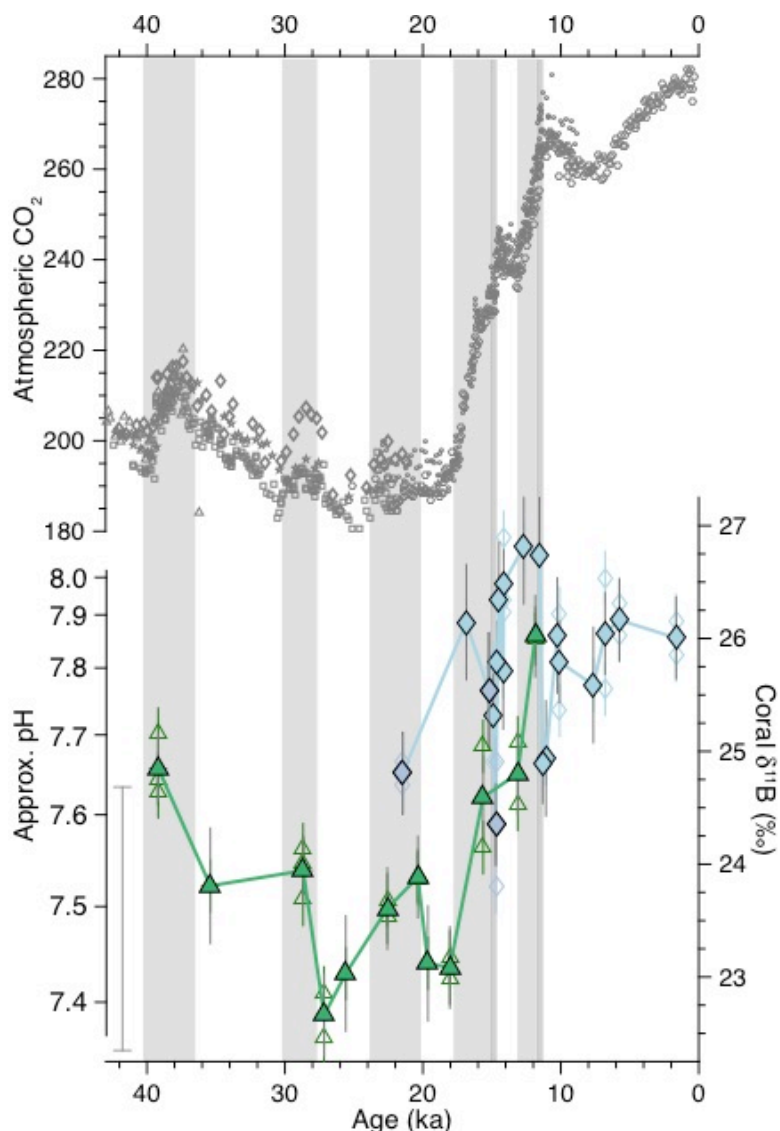
523

#### 524 **Data availability**

525 The data produced in this study is available as a supplementary table and will  
526 also be made available at the NOAA and Pangaea data repositories.

527

528 Supplementary Figures



529

530

531 **Figure S1: Deep Southern Ocean CO<sub>2</sub> chemistry and atmospheric CO<sub>2</sub>**

532 **over the last 40,000 years.** Green triangles and blue diamonds show lower

533 and upper cell deep-sea coral δ<sup>11</sup>B data respectively. Individual subsamples

534 are shown in small open symbols and mean values in larger filled symbols.

535 Error bars on individual subsamples are equivalent to 2 SD analytical

536 reproducibility and error bars on mean coral values represent 2 SE

537 uncertainty on the mean of replicate subsamples (see Methods).

538 Approximate pH values are given based on coral δ<sup>11</sup>B using the calibration in

539 Figure S5, but uncertainty on this calibration is large (inset error bar), given

540 the paucity of modern deep-sea coral data from low pH waters. Instead we

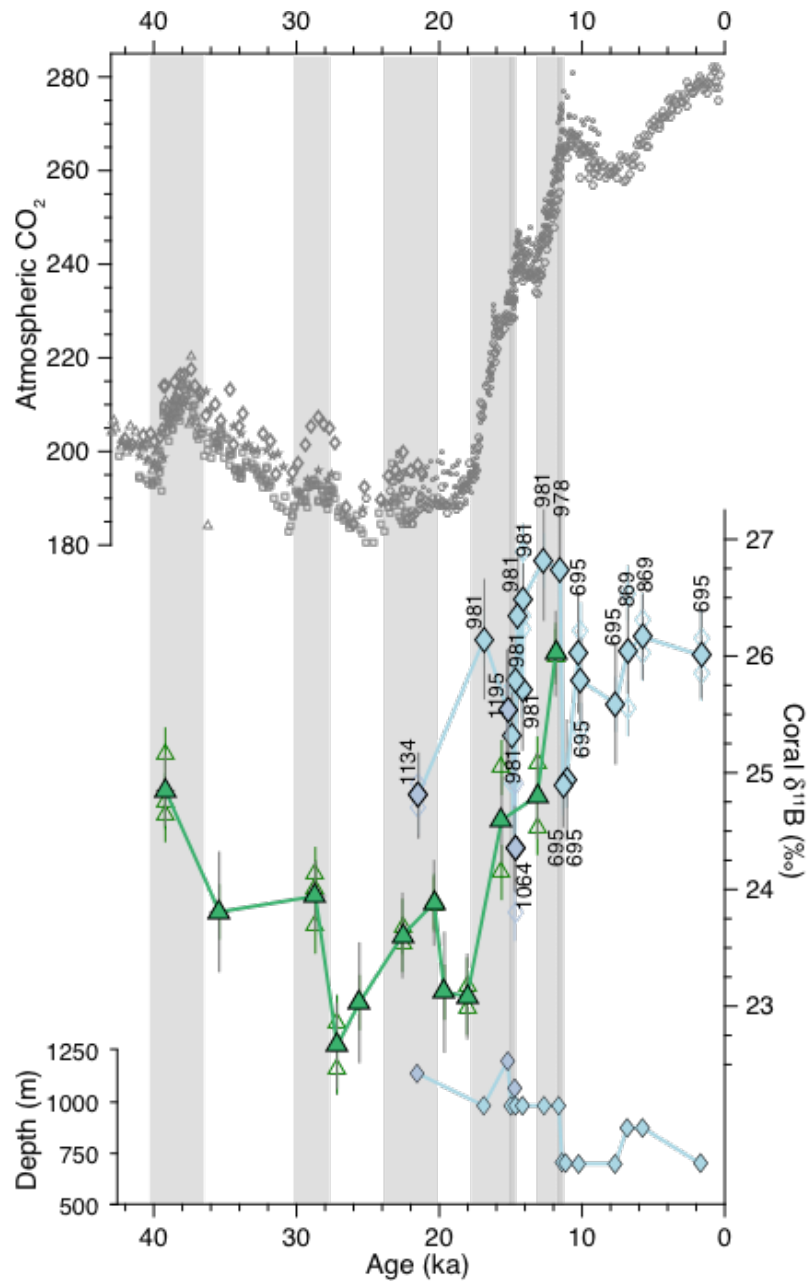
541 focus on the δ<sup>11</sup>B values themselves, which provide a proxy of carbonate

542 chemistry in their own right<sup>62</sup>. Synchronised ice core CO<sub>2</sub> data<sup>36</sup> are shown

543 in grey symbols: circles from Dome C, dots from WAIS, stars from Taylor

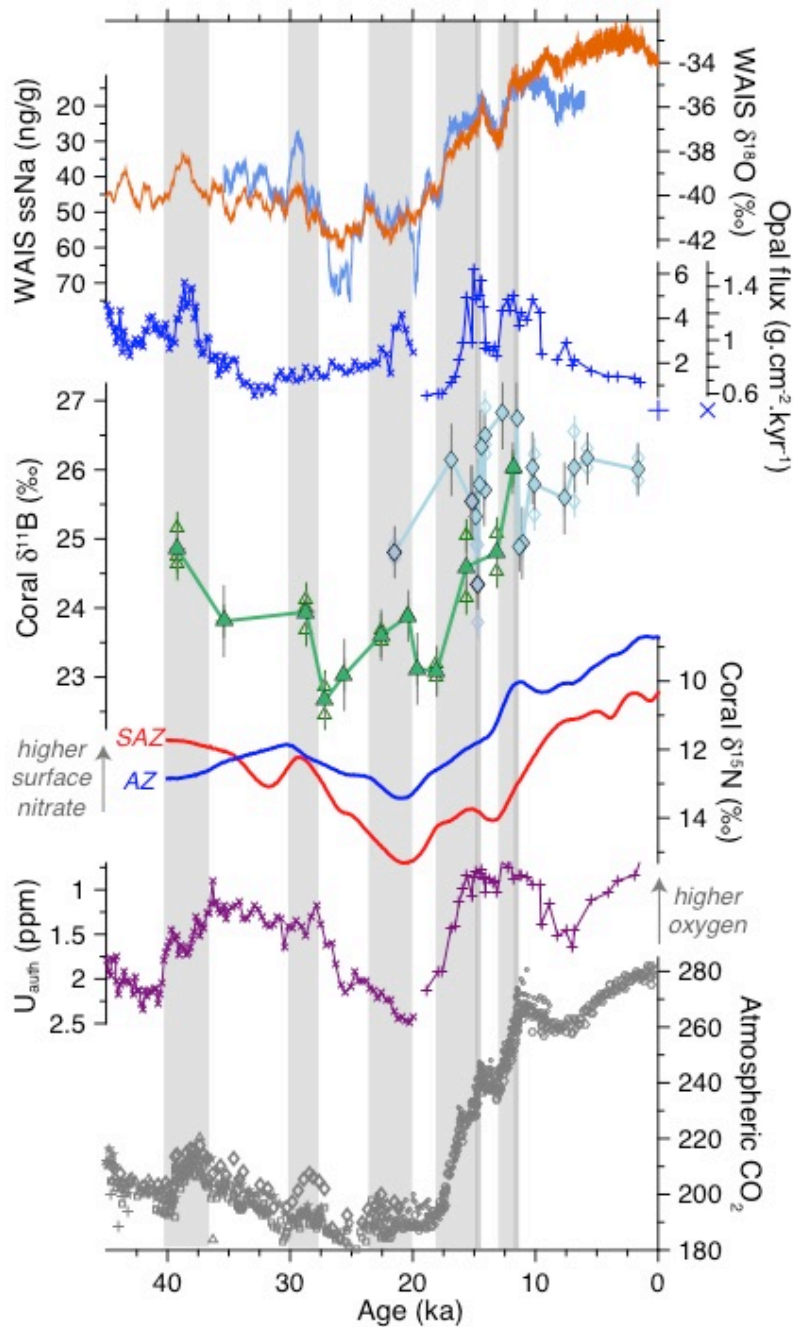
544 Dome, triangles from TALDICE, pluses from EDML, diamonds from Byrd, and

squares from Siple Dome. Grey bands highlight intervals of CO<sub>2</sub> rise.



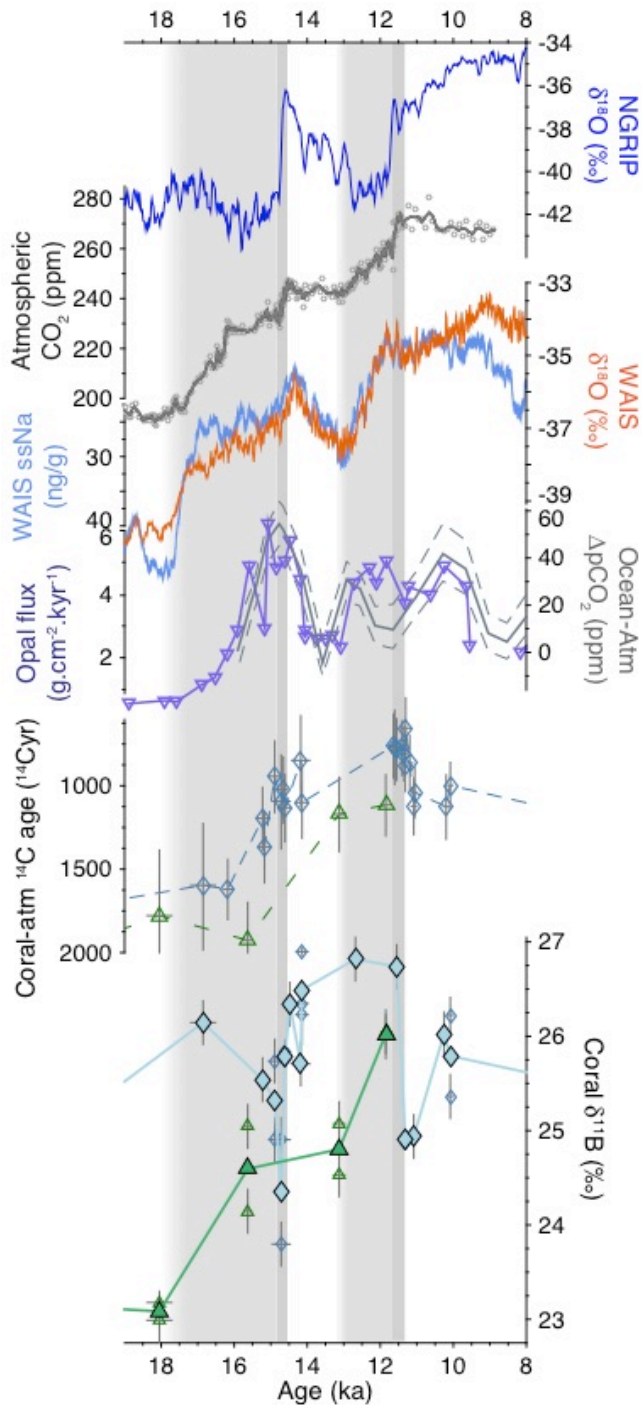
545  
 546  
 547  
 548  
 549  
 550  
 551  
 552  
 553  
 554  
 555  
 556  
 557

**Figure S2: Deep Southern Ocean CO<sub>2</sub> chemistry and atmospheric CO<sub>2</sub> over the last 40,000 years, highlighting the depths of upper cell corals.** Symbols and data are as plotted in Figure S1, but with the addition of the lower panel and annotations showing the depth in meters of each upper cell coral sample. No systematic offset is seen between samples from different depths. The only signal that occurs simultaneous with a change in depth is the decrease at ~11.5 ka, but the jump back up to higher  $\delta^{11}\text{B}$  values following this event occurs without a change in depth, giving confidence that the excursion is not a depth-related signal. Furthermore the large excursion at ~14.7 ka occurs without a significant change in depth. Note that all of the lower cell corals come from within 17 m water depth of each other.



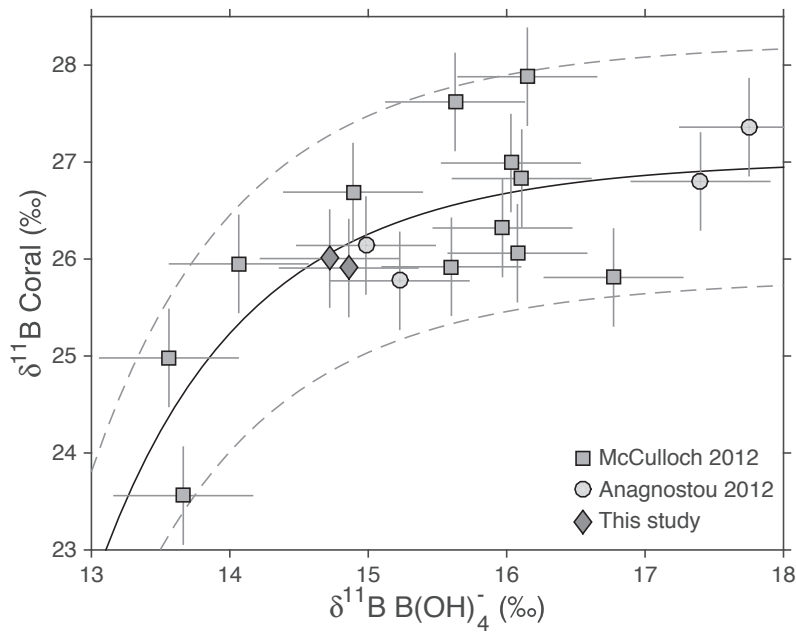
559  
 560  
 561  
 562  
 563  
 564  
 565  
 566  
 567  
 568  
 569  
 570  
 571  
 572

**Figure S3: Records of Southern Ocean biogeochemistry and CO<sub>2</sub> over the last 40,000 yr.** Data are plotted as in Figure 2, but with opal flux <sup>23</sup>, a proxy for upwelling, deep sea coral δ<sup>15</sup>N <sup>63</sup>, a proxy for surface ocean nitrate consumption, and authigenic uranium concentrations <sup>16</sup>, a proxy for bottom water redox. The opal flux and authigenic uranium records combine two sediment cores: TN057-13-4PC in the younger part of the record (pluses) and TN057-14PC in the older part of the record (crosses). The opal flux records from each core are shown on separate scales. The coral δ<sup>15</sup>N data are grouped into samples from the Antarctic Zone (AZ, blue) and Subantarctic Zone (SAZ, red). Smoothed fits to the data are shown, as provided in the original study <sup>63</sup>. Intervals of low CO<sub>2</sub> during the last ice age are associated with low upwelling, an efficient biological pump, low oxygen water rich in respired carbon, and low-pH carbon-rich water in the deep Southern Ocean.



573  
 574  
 575  
 576  
 577  
 578  
 579  
 580  
 581  
 582  
 583  
 584

**Figure S4: Deglacial records of Southern Ocean CO<sub>2</sub> chemistry and opal fluxes, and climate over Antarctica and Greenland.** Data are plotted as in Figures 2 and 3, but with opal flux<sup>23</sup>, a proxy for upwelling, surface ocean-atmosphere CO<sub>2</sub> difference, based on δ<sup>11</sup>B in planktic foraminifera<sup>26</sup>, and radiocarbon data<sup>4,25</sup> from corals within these sample groupings, shown as age offsets compared to the contemporaneous atmosphere. Intervals of rising CO<sub>2</sub> in the atmosphere are associated with input of waters rich in CO<sub>2</sub> and nutrients to the upper reaches of the Southern Ocean. Radiocarbon ages reflect the competing influences of upwelling of <sup>14</sup>C-depleted waters and improved ventilation over the deglaciation.



586

587

588 **Figure S5: Boron isotope calibration for modern *D. dianthus*.** Data are589 from open ocean sites in <sup>44,56,60</sup>, with two additional recent (<1650 yr) samples590 from the Southern Ocean from this study. Water column  $\delta^{11}\text{B}$  of borate591 ( $\text{B}(\text{OH})_4^-$ ) values are as previously published or are calculated from carbonate

592 chemistry data from nearby GLODAPv2 sites for the new samples, following

593 <sup>47,62</sup>. Note that the sensitivity of  $\delta^{11}\text{B}$  in carbonates to pH is based on the pH594 sensitivity of  $\delta^{11}\text{B}$  of borate. pH itself is not easily shown on a plot like this, as595 the relationship between  $\delta^{11}\text{B}$  of borate and pH is also somewhat influenced

596 by water temperature, salinity, and depth. A power law function was fitted to

597 the data using Matlab's curve fitting toolbox (solid line:  $\delta^{11}\text{B}_{\text{Coral}} = -1.82^{14} \times$ 598  $\delta^{11}\text{B}_{\text{B}(\text{OH})_4^-}^{-12.22} + 27.03$ ;  $R^2 = 0.57$ ). Dashed lines show the 95 % confidence

599 intervals and give a measure of calibration uncertainty as shown in the error

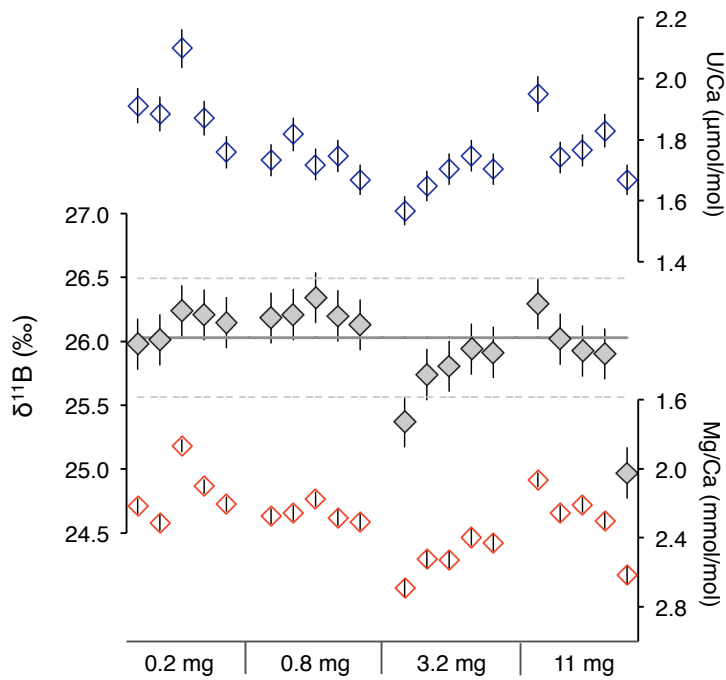
600 bar in Figure S1, though data from a given site may be able to record relative

601 changes in pH more sensitively, as seen in many paleo-proxies.

601



602



603

604

605 **Figure S6: Replicate subsamples from a *D. dianthus* septum.** To test for  
606 the potential influence of microstructural variability in composition, a coral  
607 septum was divided into 4 areas, which were then split into chunks of  
608 approximately 0.2, 0.8, 3.2 and 11 mg respectively. These were then  
609 individually crushed, cleaned, and analysed. This sample treatment was  
610 designed to preserve heterogeneity between subsamples, though note that  
611 the clustering of subsamples of a given size from a certain area of the coral  
612 may lead to that group recording a slightly different signal (as seen in the 3.2  
613 mg group). The lines in the middle panel show the mean and 2 SD, excluding  
614 one outlier in the 11 mg group.  $\delta^{11}\text{B}$  is correlated with Mg/Ca and U/Ca,  
615 showing the influence of internal variability in coral composition.

616

617

## 618 Additional References

619

- 620 34. Key, R. M. *et al.* Global Ocean Data Analysis Project, Version 2  
621 (GLODAPv2). *EPIC3ORNL/CDIAC-162, NDP-093, Carbon Dioxide*  
622 *Information Analysis Center, Oak Ridge Nat Lab* (2015).  
623 doi:10.3334/CDIAC/OTG
- 624 35. Olsen, A. *et al.* The Global Ocean Data Analysis Project version 2  
625 (GLODAPv2) – an internally consistent data product for the world  
626 ocean. *Earth System Science Data* **8**, 297–323 (2016).
- 627 36. Bereiter, B. *et al.* Revision of the EPICA Dome C CO<sub>2</sub> record from 800  
628 to 600 kyr before present. *GRL* **42**, 542–549 (2015).
- 629 37. Burke, A. *et al.* Reconnaissance dating: A new radiocarbon method  
630 applied to assessing the temporal distribution of Southern Ocean deep-  
631 sea corals. *Deep Sea Research Part I: Oceanographic Research*  
632 *Papers* **57**, 1510–1520 (2010).
- 633 38. Margolin, A. R. *et al.* Temporal and spatial distributions of cold-water  
634 corals in the Drake Passage: Insights from the last 35,000 years. *Deep*  
635 *Sea Research Part II: Topical Studies in Oceanography* **99**, 237–248  
636 (2014).
- 637 39. Spooner, P. T., Chen, T., Robinson, L. F. & Coath, C. Rapid uranium-  
638 series age screening of carbonates by laser ablation mass  
639 spectrometry. *Quaternary Geochronology* **31**, 28–39 (2016).
- 640 40. Sinclair, D. J., Kinsley, L. P. & McCulloch, M. T. High resolution analysis  
641 of trace elements in corals by laser ablation ICP-MS. *Geochim.*  
642 *Cosmochim. Acta* **62**, 1889–1901 (1998).
- 643 41. Robinson, L. F. *et al.* Primary U distribution in scleractinian corals and  
644 its implications for U series dating. *Geochem. Geophys. Geosyst.* (G3)  
645 **7**, Q05022 (2006).
- 646 42. Gagnon, A. C., Adkins, J. F., Fernandez, D. P. & Robinson, L. F. Sr/Ca  
647 and Mg/Ca vital effects correlated with skeletal architecture in a  
648 scleractinian deep-sea coral and the role of Rayleigh fractionation.  
649 *EPSL* **261**, 280–295 (2007).
- 650 43. Rollion-Bard, C., Chaussidon, M. & France-Lanord, C. Biological control  
651 of internal pH in scleractinian corals: Implications on paleo-pH and  
652 paleo-temperature reconstructions. *Comptes rendus - Geoscience* **343**,  
653 397–405 (2011).
- 654 44. Stewart, J. A., Anagnostou, E. & Foster, G. L. An improved boron  
655 isotope pH proxy calibration for the deep-sea coral *Desmophyllum*  
656 *dianthus* through sub-sampling of fibrous aragonite. *Chemical geology*  
657 **447**, 148–160 (2016).
- 658 45. Boyle, E. A. Cadmium, zinc, copper, and barium in foraminifera tests.  
659 *EPSL* **53**, 11–35 (1981).
- 660 46. Barker, S., Greaves, M. & Elderfield, H. A study of cleaning procedures  
661 used for foraminiferal Mg/Ca paleothermometry. *Geochem. Geophys.*  
662 *Geosyst.* **4**, 8407 (2003).
- 663 47. Rae, J. W. B., Foster, G. L., Schmidt, D. N. & Elliott, T. Boron isotopes  
664 and B/Ca in benthic foraminifera: Proxies for the deep ocean carbonate  
665 system. *EPSL* **302**, 403–413 (2011).

- 666 48. Foster, G. L. *et al.* Interlaboratory comparison of boron isotope analyses  
667 of boric acid, seawater and marine CaCO<sub>3</sub> by MC-ICPMS and NTIMS.  
668 *Chem. Geol.* **358**, 1–14 (2013).
- 669 49. Kiss, E. Ion-exchange separation and spectrophotometric determination  
670 of boron in geological materials. *Analytica Chimica Acta* **211**, 243–256  
671 (1988).
- 672 50. Lemarchand, D., Gaillardet, J., Göpel, C. & Manhès, G. An optimized  
673 procedure for boron separation and mass spectrometry analysis for  
674 river samples. *Chemical geology* **182**, 323–334 (2002).
- 675 51. Foster, G. L. Seawater pH, pCO<sub>2</sub> and [CO<sub>3</sub><sup>2-</sup>] variations in the Caribbean  
676 Sea over the last 130 kyr: A boron isotope and B/Ca study of planktic  
677 foraminifera. *EPSL* **271**, 254–266 (2008).
- 678 52. Al-Ammar, A. S., Gupta, R. K. & Barnes, R. M. Elimination of boron  
679 memory effect in inductively coupled plasma-mass spectrometry by  
680 ammonia gas injection into the spray chamber during analysis.  
681 *Spectrochimica Acta Part B: Atomic Spectroscopy* **55**, 629–635 (2000).
- 682 53. Misra, S., Owen, R., Kerr, J. & Greaves, M. Determination of δ<sup>11</sup>B by  
683 HR-ICP-MS from mass limited samples: Application to natural  
684 carbonates and water samples. *Geochemica et Cosmochimica Acta*  
685 **140**, 531–552 (2014).
- 686 54. Rae, J. W. B. in *Boron Isotopes* 107–143 (Springer, 2018).
- 687 55. McCulloch, M. T. *et al.* in *Boron Isotopes* 145–162 (Springer, 2018).
- 688 56. Anagnostou, E., Huang, K. F., You, C. F., Sikes, E. L. & Sherrell, R. M.  
689 Evaluation of boron isotope ratio as a pH proxy in the deep sea coral  
690 *Desmophyllum dianthus*: Evidence of physiological pH adjustment.  
691 *EPSL* **349-350**, 251–260 (2012).
- 692 57. Trotter, J. *et al.* Quantifying the pH 'vital effect' in the temperate  
693 zooxanthellate coral *Cladocora caespitosa*: Validation of the boron  
694 seawater pH proxy. *EPSL* **303**, 163–173 (2011).
- 695 58. Venn, A. A. *et al.* Impact of seawater acidification on pH at the tissue-  
696 skeleton interface and calcification in reef corals. *PNAS* **110**, 1634–  
697 1639 (2013).
- 698 59. Allison, N., Cohen, I., Finch, A. A., Erez, J. & Tudhope, A. W. Corals  
699 concentrate dissolved inorganic carbon to facilitate calcification. *Nature*  
700 *Communications* **5**, 5741 (2014).
- 701 60. McCulloch, M. *et al.* Resilience of cold-water scleractinian corals to  
702 ocean acidification: Boron isotopic systematics of pH and saturation  
703 state up-regulation. *Geochemica et Cosmochimica Acta* **87**, 21–34  
704 (2012).
- 705 61. Gagnon, A. C., Adkins, J. F., Erez, J. & Eiler, J. M. Sr/Ca sensitivity to  
706 aragonite saturation state in cultured subsamples from a single colony  
707 of coral: Mechanism of biomineralization during ocean acidification.  
708 *Geochemica et Cosmochimica Acta* **105**, 240–254 (2013).
- 709 62. Rae, J. W. B. in *Boron Isotopes* 107–144 (2017).
- 710 63. Wang, X. T. *et al.* Deep-sea coral evidence for lower Southern Ocean  
711 surface nitrate concentrations during the last ice age. *PNAS* **114**, 3352–  
712 3357 (2017).
- 713